JOURNAL OF GEOPHYSICAL RESEARCH, VOL. 110, C02019, doi:10.1029/2004JC002467, 2005

Generation of secondary internal waves by the interaction of an internal solitary wave with an underwater bank

Vasiliy Vlasenko
School of Earth, Ocean and Environmental Sciences, University of Plymouth, Plymouth, UK

Werner Alpers
Zentrum für Meeres- und Klimaforschung, Institut für Meereskunde, Universität Hamburg, Hamburg, Germany

Received 6 May 2004; revised 17 October 2004; accepted 20 December 2004; published 22 February 2005.

[1] The generation of secondary internal waves by the interaction of a large-amplitude internal solitary wave with the Dreadnought Bank in the Andaman Sea (6°40′N, 95° 47′E) is shown by analyzing a synthetic aperture radar (SAR) image acquired by the European Remote Sensing satellite ERS-2 and by carrying out model calculations. Although the Dreadnought Bank is quite deep (241 m), the model calculations show that large-amplitude internal solitary waves as encountered in this sea area can overturn and break over the bank and generate secondary internal waves. Comparison of model results with observations clearly demonstrates that the semicircular wave pattern visible on the ERS-2 SAR image centered at the Dreadnought Bank is indeed a sea surface manifestation of a secondary internal wave packet generated by scattering of a large-amplitude internal solitary wave and not by the interaction of the barotropic tidal flux with this underwater obstacle.

Citation: Vlasenko, V., and W. Alpers (2005), Generation of secondary internal waves by the interaction of an internal solitary wave with an underwater bank, *J. Geophys. Res.*, *110*, C02019, doi:10.1029/2004JC002467.

1. Introduction

[2] The generation of internal solitary waves by the interaction of tidal currents (barotropic tidal flows) with underwater topographic features, like continental slopes, sills, ridges or underwater banks, has been investigated extensively theoretically as well as experimentally [*Maxworthy*, 1979; *Lamb*, 1994; *Gerkema and Zimmermann*, 1995; *Brandt et al.*, 1996, 1997]. The interaction of solitary waves with a sloping bottom has also been the subject of many theoretical and experimental studies [*Kao et al.*, 1985; *Wallace and Wilkinson*, 1988; *Helferich*, 1992; *Liu et al.*, 1998; *Vlasenko and Hutter*, 2002a]. However, to our knowledge, the interaction of internal solitary waves with a sill has only been studied in laboratory experiments [*Diebels et al.*, 1994; *Wessels and Hutter*, 1996; *Huettemann and Hutter*, 2001].

[3] We have observed on a synthetic aperture radar (SAR) image acquired by the European Remote Sensing satellite ERS-2 over the Andaman Sea, surface manifestations of a packet of strong internal solitary waves in which a smaller-scale semicircular weak internal wave packet is embedded. Comparison with a bathymetric map reveals that the focal point of this small-scale wave pattern coincides with the shallowest point of the Dreadnought Bank, which has a depth of 241 m and is located at 6°40′N, 95°47′E. We hypothesize that this internal wave packet was generated by the interaction of a strong solitary wave with the Dreadnought Bank. However, another possibility is that it was generated directly by the interaction of the barotropic tide with this underwater bank. In this paper we show by carrying out numerical simulations and by comparing the results of the simulations with the ERS-2 SAR image, that it was generated by the breaking of a large-amplitude internal solitary wave over the underwater bank. Breaking occurs when the horizontal orbital velocity associated with the internal solitary wave exceeds the local phase speed (for details see section 5). As input data to our model calculations, we use historical data of the stratification of the water column, the barotropic tidal flux and the amplitude of the primary internal solitary waves in the southern section of the Andaman Sea.

2. Observational Data

[4] Figure 1 shows a section of an ERS-2 SAR image acquired over the Andaman Sea during orbit 9477 on 11 February 1997 at 0360 UTC. From the full ERS-2 SAR strip (not shown here) we infer that the large-scale linear wave pattern is the sea surface manifestation of a strong internal solitary wave packet which was generated by the interaction of the barotropic tide with shallow bottom topographic features located between Sumatra and the Great Nicobar Island. Figure 2 shows a zoom of the ERS-2 SAR

0148-0227/05/2004JC002467$09.00

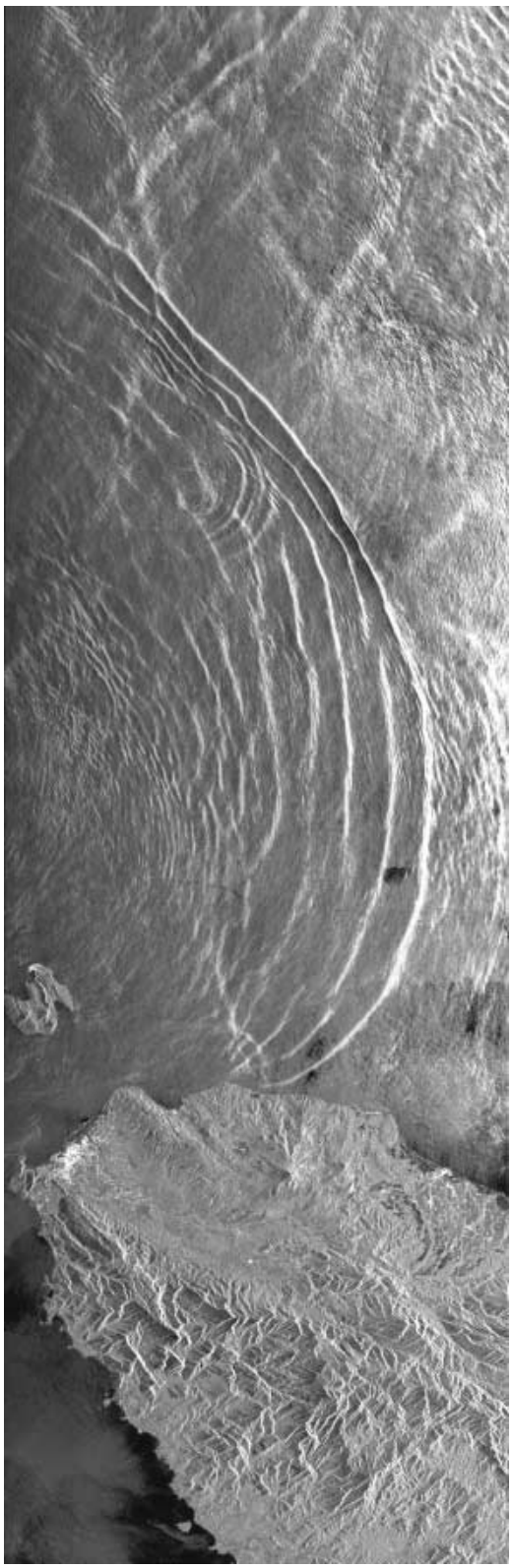

Figure 1. ERS-2 synthetic aperture radar (SAR) strip acquired over the Andaman Sea during orbit 9477 (frames 3465, 3483, and 3501) on 11 February 1997 at 0360 UTC showing sea surface manifestations of internal solitary waves. The northwestern section of Sumatra and the Indonesian island Weh are visible. The imaged area is 100 × 300 km. Copyright: ESA.

image depicted in Figure 1 on the section where the secondary internal wave packet was generated.

[5] The comparison of the ERS SAR image (Figures 1 and 2) with a sea map (Figure 3) reveals that the focal point of the semicircular small-scale wave pattern is located at 6°40′N, 95°47′E, which is the position of the shallowest point of the Dreadnought Bank (241 m). Figure 4 shows a detailed bathymetric map of this site with the sea surface manifestations of the incident internal solitary waves (dashed thick lines) and of the scattered secondary internal waves (thin dotted lines) visible on the ERS-2 SAR image (Figure 2). Thus this underwater bank must be instrumental in the generation process of the semicircular internal solitary wave packet. In this image we can measure the distances between the focal point and the leading solitons in both packets. The distance to the leading soliton in the large-scale wave packet is 22.5 km, and the distance to the leading soliton in the small-scale wave packet varies between 15 km and 17 km (depending on direction). These measured distances will be compared in section 6 with the corresponding distances calculated from the model.

3. Model

[6] The generation of internal waves by the interaction of baroclinic tides with shallow underwater features, like sills or seamounts, as well as the interaction of intense internal solitary waves with these underwater features is a three-dimensional (3-D) process. In our case it would be appropriate to describe the wave-topography interaction in the framework of a 3-D fully nonlinear and nonhydrostatic system of hydrodynamic equations. Unfortunately, the existing modern 3-D numerical models of baroclinic tides [see, e.g., *Holloway and Merrifield*, 1999; *Niwa and Hibiya*, 2001; *Cummins et al.*, 2001] usually exploit the hydrostatic approximation for pressure. Using a 3-D non-hydrostatic mesoscale oceanic model [*Mahadevan et al.*, 1996; *Marshall et al.*, 1997; *Casulli and Stelling*, 1998] for the study of the dynamics of highly nonlinear internal

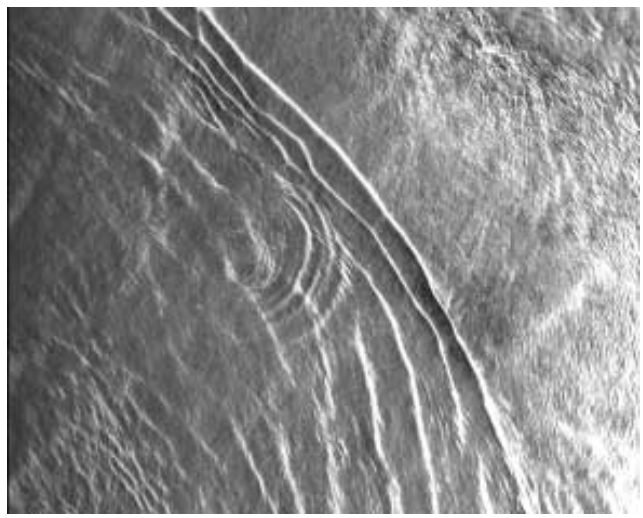

Figure 2. Zoom of the ERS-2 SAR image of the sea area around the Dreadnought Bank. The imaged area is 100 × 80 km. Copyright: ESA.

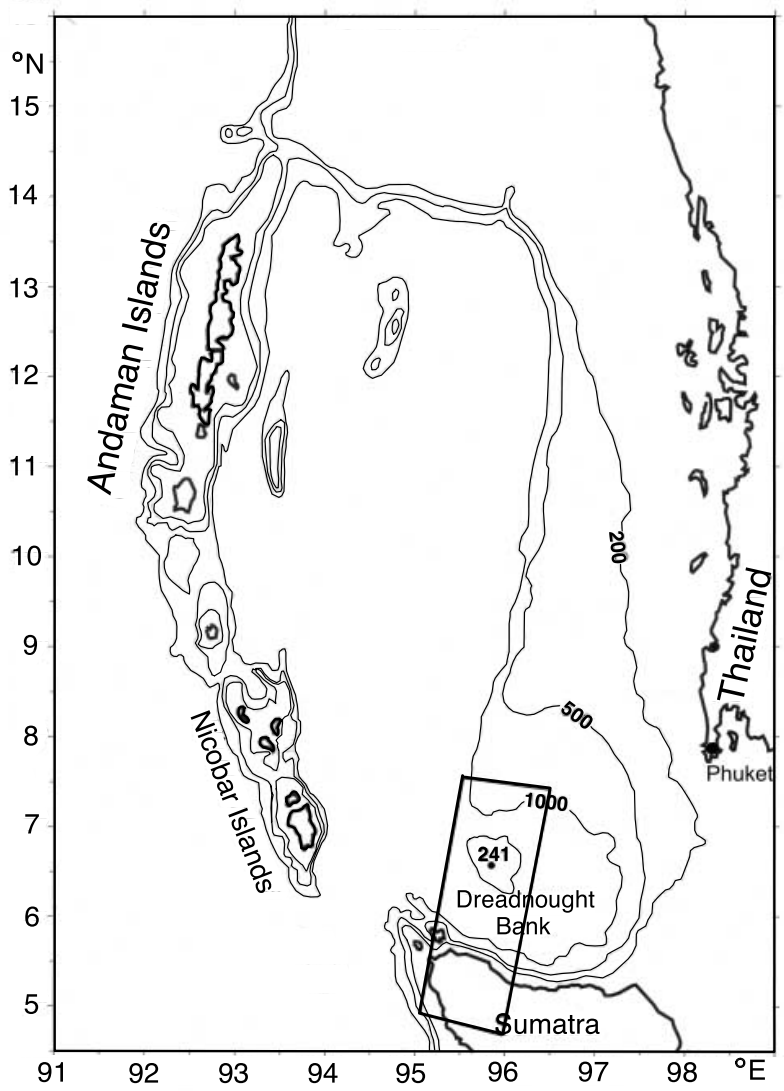

Figure 3. Bathymetric map of the Andaman Sea. Bold lines represent the shorelines, and thin lines represent the isobaths. The numbers denote depth in meters. The rectangular insert shows the location of the ERS-2 SAR strip depicted in Figure 1.

wave causes great problems because of the high demand on spatial and temporal steps in the computing. However, even in the 2-D case it is very difficult to model the interaction of an internal wave with underwater bottom topography numerically. The application of the most advanced numerical 2-D models gives satisfactory results only when using fine-resolution grids (spatial step: several meters) [*Vlasenko and Hutter*, 2002a, 2002b]. Since our study is not aimed at describing all details of this interaction, but only aimed at answering the principle question as to which of the two possible mechanisms is responsible for the generation of secondary internal waves at the Dreadnought Bank, we use a fine-resolution 2-D nonhydrostatic model which is based on the incompressible 2-D Reynolds equations. Our results can be considered as approximations, in particular, the calculated amplitudes of the scattered internal solitary waves constitute only upper bounds for the wave amplitudes. Thus 3-D effects, like refraction and radial spreading, are not included in our model. However, by using a linear model, we shall give some estimates how these 3-D effects affect the results (section 4.2).

[7] The computational area (model domain) consists of a basin of constant depth, H_0 = 900 m, containing the local bottom elevation located in zone II ($-l < x < l$, $-\infty < y < \infty$ (see Figure 5)) with a peak of 241 m below the sea surface corresponding to the shallowest point of the Dreadnought Bank. The water depth H_2 in zone II is assumed to be independent of the y coordinate ($\partial H_2/\partial y \equiv 0$). The basin is filled with continuously stratified water whose stationary density profile $\rho_0(z)$ (or its buoyancy frequency distributions $N(z)$, see Figure 6) is close to the one measured in the Andaman Sea in winter [*Levitus and Boyer*, 1994; *Levitus et al.*, 1994].

[8] The aim of this investigation is to answer the question whether the secondary internal waves, whose sea surface manifestations visible on the ERS-2 SAR image depicted in

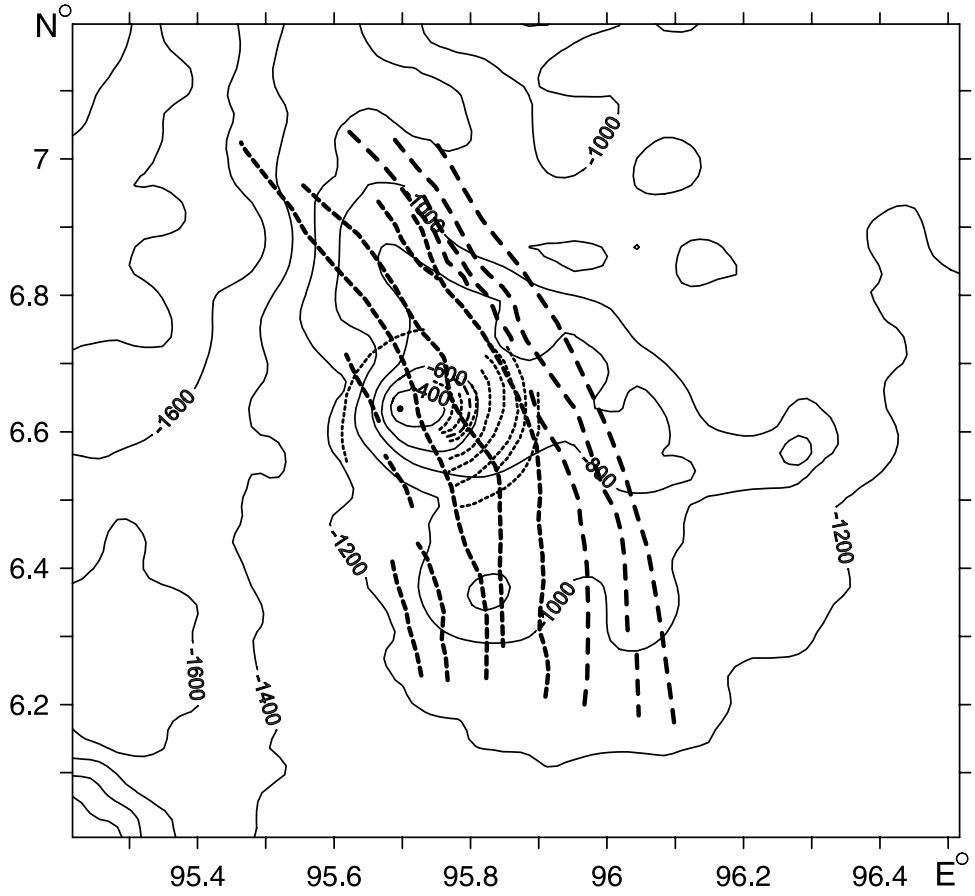

Figure 4. Detailed bathymetric map of the sea area around the Dreadnought in the Andaman Sea. Bold dashed lines denote the sea surface manifestations of the incident internal solitary waves, and thin dotted lines denote the secondary scattered internal waves visible on the ERS-2 SAR image depicted in Figures 1 and 2.

Figures 1 and 2, are generated by scattering of an internal solitary wave (ISW) at the bank (problem I) or by interaction of the baroclinic tide with the bank (problem II).

[9] The two-dimensional system of Reynolds equations in the Boussinesq approximation, written in Cartesian (x, y, z) coordinates in which the x and y axis lie on the undisturbed free surface and the z axis points upward (opposite to the direction of gravity), reads

$$\begin{aligned}\omega_t + J(\omega,\psi) - fv_z &= g\widetilde{\rho}_x/\rho_a + (a_h\psi_{xz})_{xz} + (a_h\psi_{xx})_{xx} + (a_z\psi_{zz})_{zz} \\ &\quad + (a_z\psi_{xz})_{xz}, \\ v_t + J(v,\psi) + f\psi_z &= (a_h v_x)_x + (a_z v_z)_z, \\ \widetilde{\rho}_t + J(\widetilde{\rho},\psi) + \rho_a g^{-1} N^2(z)\psi_x &= (k_h\widetilde{\rho}_x)_x + \left[k_z(\rho_0+\widetilde{\rho})_z\right]_z.\end{aligned} \tag{1}$$

Here ($u = \psi_z$, $w = -\psi_x$) denotes the stream function, u, v, w denote the horizontal and vertical velocity components, and $\omega = \psi_{xx} + \psi_{zz}$ denotes the vorticity function. Furthermore, f denotes the Coriolis parameter, k_h and k_z denote the coefficients of vertical and horizontal turbulent diffusion, a_h and a_z the coefficients of vertical and horizontal eddy viscosity, $N^2(z) = -g\rho_a^{-1}d\rho_0/dz$ denotes the buoyancy frequency, and $J(a, b) = a_x b_z - a_z b_x$ is the Jacobian operator. The subscripts x, z, t denote (with the exception of k_z and a_z) partial derivatives with respect to these variables. The water density $\rho(x, z, t)$ is written here as the sum of a stationary background density $\rho_0(z)$ and a density fluctuation $\widetilde{\rho}(x, z, t)$ associated with the wave disturbances.

[10] We use for the coefficients of vertical turbulent exchange, a_z and k_z, the Richardson number parameterizations [*Pakanowski and Philander*, 1981]:

$$\begin{aligned}a_z &= \frac{a_0}{(1+\alpha Ri(x,z,t))^p} + a_b \\ k_z &= \frac{a_z}{(1+\alpha Ri(x,z,t))^p} + k_b.\end{aligned} \tag{2}$$

The Richardson number $Ri(x, z, t)$ depends on the local buoyancy frequency $N(x, z, t)$ and the local vertical velocity shear $u_z(x, z, t)$ as follows:

$$Ri(x,z,t) = \begin{cases} N^2(x,z,t)/u_z^2(x,z,t), & \text{if } \rho_z < 0, \\ 0, & \text{if } \rho_z > 0. \end{cases}$$

[11] Here a_b and k_b are dissipation parameters describing background turbulence, and a_0, α and p are adjustable parameters. These parameterizations of the vertical turbulent kinematic viscosity and diffusivity increase the coefficients a_z and k_z in regions with small values of Ri. In

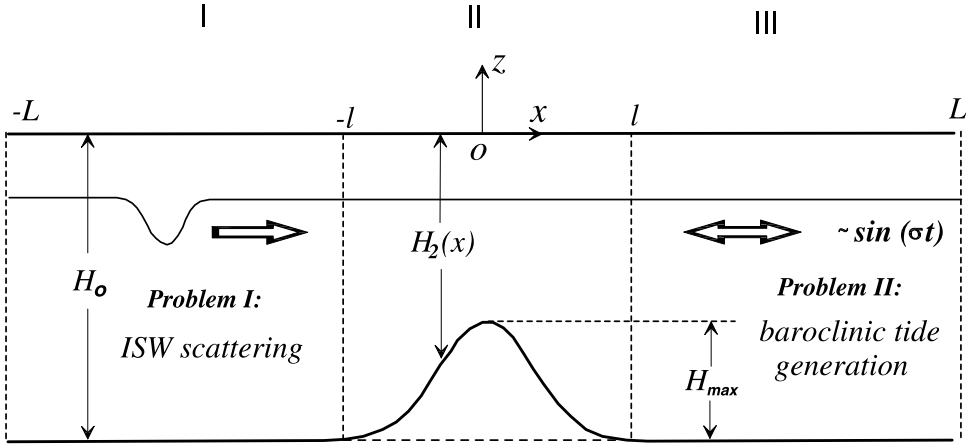

Figure 5. Schematic of the computational area, with a sketch of the two basic mechanisms of internal wave generation (problem I and problem II). The sea surface is at $z = 0$, and the depth of the basin is H_0. The underwater bank extends from $x = -l$ to $x = l$, has a depth of $H_2(x)$, and at the shallowest point, has a depth of $H_0 - H_{\max}$. The tidal forcing has the frequency σ.

regions with vertical density inversion due to wave breaking, the Richardson number is set equal to 0.

[12] For the coefficients of horizontal turbulent exchange, a_h and k_h, we use the parameterization of *Stacey and Zedel* [1986]:

$$a_h = \beta_0 + \beta(\Delta x)^2|\partial u/\partial x|, \qquad k_h = \mu_0 + \mu(\Delta x)^2|\partial u/\partial x|. \tag{3}$$

Here β_0 and μ_0 refer to the homogeneous background, β and μ are adjustable parameters, and Δx is the step size of the horizontal grid.

[13] In this paper, two sets of initial and boundary conditions are applied depending on the two generation mechanisms: the generation of internal waves by barotropic tidal flux over the underwater bank (case 1) or by scattering of an internal solitary wave by the underwater bank (case 2). Common to both cases are the boundary conditions at the free surface and at the bottom. Since we want to study the baroclinic response of the ocean, the "rigid-lid" condition at $z = 0$ can be used:

$$\psi = \omega = \widetilde{\rho}_z = v_z = 0. \tag{4}$$

The first condition says that the free surface is a streamline, and the last two conditions say that at the free surface the mass flux and the shear stress vanish. The second condition for the vorticity, $\omega = 0$, implies that at the sea surface tangential stress (wind forcing) is zero.

[14] The bottom line, $z = -H(x)$, is a streamline on which the "no-slip" condition and zero mass flux across the boundary is imposed. This yields

$$\psi = \Psi_0 \sin(\sigma t), \quad \omega = \omega_0, \qquad v = \psi_x = \psi_z = 0, \quad \widetilde{\rho}_n = 0, \tag{5}$$

where $\partial/\partial n$ denotes the derivative normal to the bottom, Ψ_0 denotes the amplitude of the vertically integrated water flux in the barotropic tidal wave, and σ denotes the tidal frequency. In the case of internal wave scattering, Ψ_0 is set equal to zero. The value of the vorticity at the bottom, ω_0, is calculated from the stream function at the previous temporal layer. Initial fields and the boundary conditions at lateral liquid boundaries of the computational area are discussed below. Some more details about the numerical procedure can be found in the work of *Vlasenko and Hutter* [2002a, 2002b] and *Vlasenko et al.* [2002].

[15] Several numerical experiments were carried out for determining grid steps and optimum values for the eddy viscosity and the turbulent diffusivity parameters. We found that the numerical scheme was stable even during the overturning of a wave front if we chose the following values for these parameters: $\Delta t = 0.5$ s, $\Delta x = 2$ m, $\Delta z = 3$ m

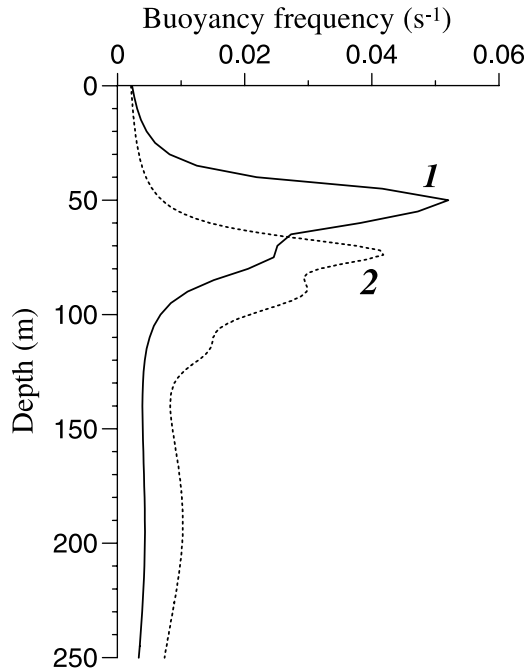

Figure 6. Smoothed buoyancy frequencies (1) and (2), typical for the Andaman Sea.

in the deep part of the basin and $\Delta z \cong 0.5$ m over the top of the bank. In accordance with measurements and estimates of the background viscosity and diffusivity, a_b and k_b, given by *Sandstrom and Oakey* [1995], we chose the value 10^{-4} m^2 s^{-1} for both parameters. Such low level of dissipation allows the internal solitary waves to propagate over large distances without significant attenuation (distances of 500 wavelengths and more). This is in agreement with in situ observations, which show that internal solitary waves can propagate several hundred kilometers from their source of generation without significant attenuation [*Osborne and Burch*, 1980; *Apel et al.*, 1985]. The other parameters used in our calculations have the values: $a_0 = 10^{-2}$ m^2 s^{-1}, $p = 2$, $a = 4$, $\beta_0 = 10^{-4}$ m^2 s^{-1}, $\mu_0 = 10^{-5}$ m^2 s^{-1}, and $\beta = \mu = 1$.

4. Generation of Internal Waves by Barotropic Tide

[16] First we investigate whether it is possible that the observed semicircular wave packets in the ERS SAR image can result from the interaction of a barotropic tidal flux with the Dreadnought Bank. As stated before, since our model is two-dimensional, it cannot account for the radial divergence of wave energy from the source of generation. During such a spreading, the amplitudes of the radiating waves attenuate with distance from the bank. Thus in our 2-D model the amplitudes of the radiating secondary waves are always overestimated and therefore our model results constitute upper bounds for the wave amplitudes.

4.1. Nonlinear Two-Dimensional (2-D) Model: Estimation of Amplitudes

[17] The model is initialized by a barotropic tidal flux oscillating with the tidal frequency σ (see Figure 5, problem II). It interacts with the underwater bank and generates internal waves which propagate away from the source in both directions. Since we want to calculate only the baroclinic response of the ocean caused by tidal flow over a localized bottom topography, we can prescribe the "zero" initial conditions at the initial moment $t = 0$ in the whole area, if we assume the absence of baroclinic disturbances before that time as

$$\psi = \omega = \widetilde{\rho} = 0 \quad v = -(f/\sigma)\Psi_0/H_0(x). \tag{6}$$

The only type of motion which can exist at $t = 0$ is the along-topography tidal flux represented by the v component of the barotropic tidal flow velocity. In the viscous case these conditions are valid with good accuracy for variable bottom topography through the whole water column, except in a thin bottom boundary layer.

[18] First we define the boundary conditions at the liquid lateral boundaries at $x = \pm L$ (see Figure 5). We are concerned with the generation of internal waves in a restricted area, i.e., in the band $x < -l$. Outside of this area, i.e., in the band $x > l$, the basin depth is constant. Other sources of wave generation are absent. In this case the flow field can be written as the sum of a barotropic tidal flux and a perturbation field associated with internal waves propagating away from the source of generation. Taking this in mind, the following conditions have to be satisfied at the boundaries $x = \pm L$:

$$\begin{aligned} \psi(\pm L, z, t) &= -(z/H_0)\Psi_0 \sin(\sigma t), \quad \widetilde{\rho} = 0 \\ v(\pm L, z, t) &= -f/(\sigma H_0)\Psi_0 \cos(\sigma t), \quad \omega = 0. \end{aligned} \tag{7}$$

Here the signs "−" and "+" refer to the boundaries at the left- and right-hand sides, respectively. These conditions imply the presence of only barotropic wave motions at the liquid boundaries with tidal ellipses aligned in the direction normal to the underwater bank. Their ellipticity is given by the ellipticity factor f/σ (ratio of the semiaxes). This assumption can be justified because there is an upper limit for the velocity of the baroclinic tidal disturbances. In the ocean, this velocity does usually not exceed 2–2.5 m s^{-1}. The trick is to set the model boundaries sufficiently far away from the internal wave source ($l \ll L$) such that the leading waves generated in region II at $|x| < l$ reach the boundary only after several wave periods. During this time the fluid motions in the vicinity of the bottom topography are unaffected by the presence of the lateral boundaries.

[19] We have solved equations (1) and (4)–(7) numerically. Even though the ERS-2 SAR image was acquired in winter (11 February), we have carried simulations for two different vertical profiles of the buoyancy frequency, $N(z)$, which are representative for winter and summer conditions (see Figure 6). This is done in order to study the sensitivity of the model results to the water stratification. For the same reason we have carried out simulations for two different 2-D model bottom topographies of the Dreadnought Bank: one 2-D model topography is obtained by making a cut through the 3-D bottom topography (see Figure 4) intersecting the top in east-west direction and another one by making a cut one in north-south direction. Furthermore, we have carried out simulations for two different tidal forcings representative for neap and spring tides, $\Psi_0 = 20$ m^2 s^{-1} and $\Psi_0 = 50$ m^2 s^{-1}, respectively. In these simulations we have held constant the parameters of the turbulent exchange and chosen the following values: $a_h = k_h = 0.1$ m^2 s^{-1}, $a_z = k_z = 10^{-4}$ m^2 s^{-1}(according to *Sandstrom and Oakey* [1995]).

[20] The results of the simulations for the two values Ψ_0 are depicted in Figure 7. The disturbances of the anomalies of the conventional density field at the time $t = 2T$ ($T = 12.4$ h is the tidal period) are plotted. In these simulations the buoyancy frequency profile depicted in Figure 6 as line 1 was used. The simulations for the other profile (line 2) yields similar results (not reproduced here).

[21] These simulations show that the wave disturbances induced by the interaction of the barotropic tidal flow over the underwater bank are very weak; their amplitudes are only a few meters. They are much weaker than the wave disturbances induced by the interaction of a strong internal solitary wave with this bank as will be shown in the next section. The reason for this weak response of the density field to the barotropic forcing is that the Dreadnought Bank is much deeper than the depth of the pycnocline (see Figure 6).

[22] An interesting side result of these simulations is that, in the case of strong tidal forcing, also internal wave trains of the second baroclinic mode are generated. Three wave

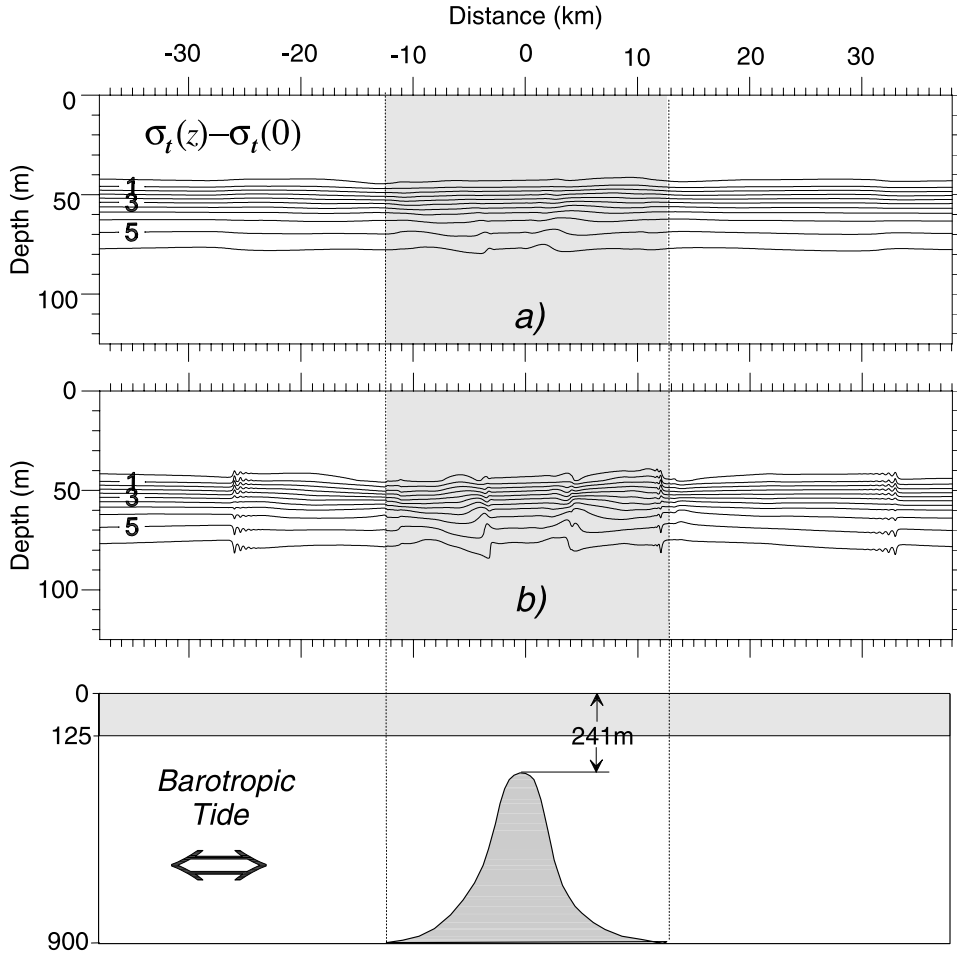

Figure 7. Anomalies of the conventional density field generated by the barotropic tidal flow over the underwater bank for (a) moderate (Ψ_0 = 20 m^2 s^{-1}) and (b) strong (Ψ_0 = 50 m^2 s^{-1}) tidal forcing. The fields were calculated for the buoyancy frequency profile depicted in Figure 6 as line 1. Only the disturbances of the upper 125 meter layer are shown. The plots represent the disturbances at the time $t = 2T$, i.e., after two tidal cycles.

packets of this kind can clearly be delineated in the plot depicted in Figure 7b. The reason for their generation can easily be explained in the framework of our model, but this is beyond the scope of the present paper. We only note here that the spatial characteristics of these wave packets are not in agreement with the SAR observations. The distance between two successive waves in the wave packets is several hundred meters, whereas the corresponding distance observed in the SAR image is one order of magnitude larger (several kilometers). Thus the observed secondary wave packet visible in the ERS SAR image cannot result from such a generating mechanism.

4.2. Linear Two-Layer Model: Estimation of 3-D Effects

[23] In reality, the topography of the Dreadnought Bank resembles much more an ellipse than a ridge, which implies that radial spreading can reduce the wave amplitude considerably when the wave propagates away from the source of generation. In addition, the wave field generated over such a topography has a much more complicated spatial structure than the wave field generated over a ridge. In order to obtain estimates of these three-dimensional effects we use a 3-D two-layer linear. The equations and the method of solving them numerically are described in the Appendix. In the calculations the following parameters were used: H_1 = 60 m, H_2 = 1200 m, and γ = 0.994. The 3-D topography of the Dreadnought Bank has been extracted from the 2′ resolution bottom topography map (see http://www.ngdc.noaa.gov/mgg/gdas/gd des-ignagrid.html) shown in Figure 4.

[24] One result of the simulations carried out with this linear model is depicted in Figure 8. The oval-shaped pattern in the center having different gray scales represents the amplitude of the internal wave disturbance normalized to its maximum value. The plot shows two local maxima of the tidally generated waves which are located at the lateral boundaries of the bank where the gradient of the bottom topography have local maxima. As a consequence, the barotropic tide generates a maximum baroclinic response here. Note that the maxima do not coincide with the top of the bank, which contradicts the assumption that the shallowest point of the Dreadnought Bank is a single source for the generation of secondary internal waves. Furthermore, Figure 8 shows that the tidally generated internal wave

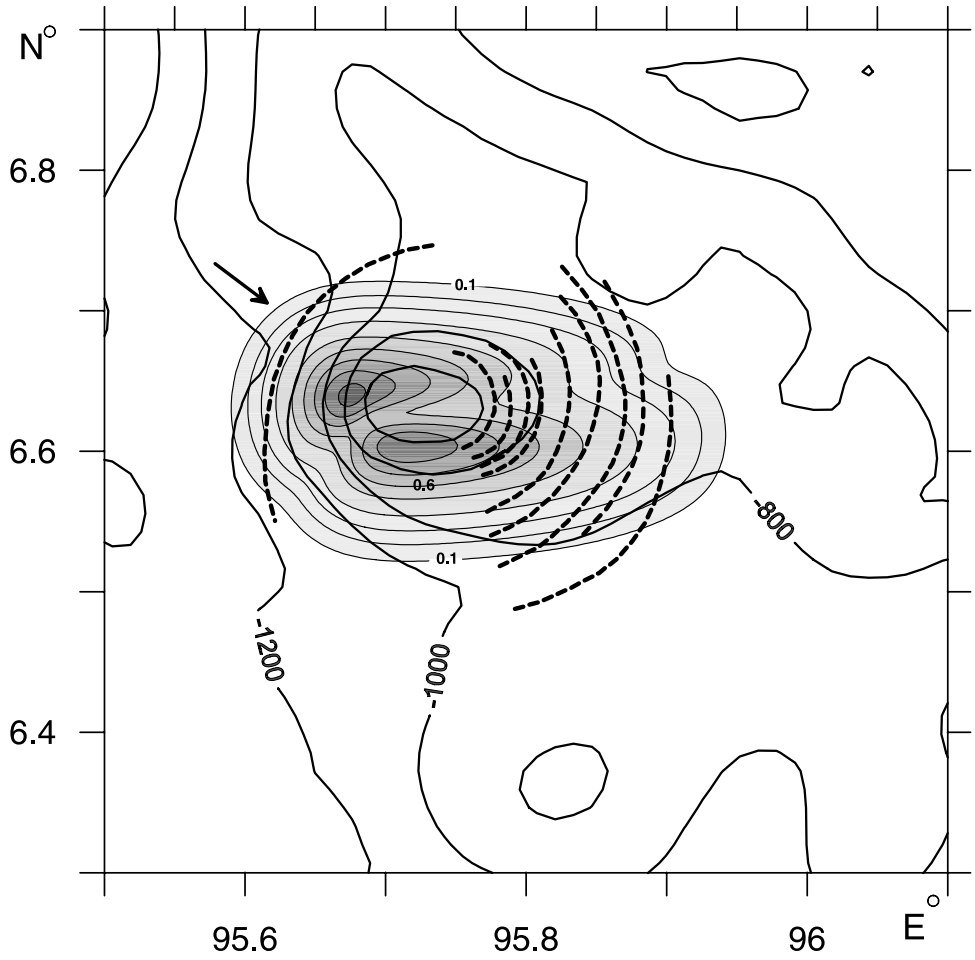

Figure 8. Amplitudes of the interface displacements generated by the interaction of the barotropic tide with the Dreadnought Bank as calculated from a two-layer linear model. The gray scales and the isolines denote the amplitudes of the internal wave disturbances normalized to their maximum value (contour interval equals 0.1). Inserted are the isobaths (solid lines, depth in meters) and the sea surface manifestations of the secondary internal waves (dashed lines).

disturbance radiates in all directions from the bank's center to the periphery. At the bottom of the bank the amplitude has already dropped to 0.1–0.2 of its peak value.

5. Generation of Secondary Internal Waves by Scattering of an Internal Solitary Wave

[25] Now we investigate whether it is possible that the observed semicircular wave packets in the ERS SAR image can result from the interaction of a large amplitude internal solitary wave (ISW) with the Dreadnought Bank.

[26] In the simulations we assume that a plane internal solitary wave depression with amplitude a_m, whose vertical structure is defined by its density profile, propagates from the deep section of the Andaman Sea toward the Dreadnought Bank (Figure 5, problem I). The measured amplitudes of internal solitary waves in the Andaman Sea vary considerably and can attain values (peak-to-trough) of up to 100 m. The first measurements of such large waves were performed by *Perry and Shimke* [1965], who measured with a bathythermograph an internal solitary wave with an amplitude of 80 m. Later, *Osborne et al.* [1978] and *Osborne and Burch* [1980] observed in current meter measurements carried out in the Andaman Sea several packets of internal solitary waves that had amplitudes (peak-to-trough) of up to 100 m and current speeds in excess of 1 m s^{-1}. More recent observation of large internal solitary waves in the Andaman Sea with amplitudes of about 50 m were reported by *Alpers* [2002]. In order to investigate how the generation of secondary internal waves depends on wave amplitude, we have carried out simulations for several amplitudes in the range between 10 and 85 m.

[27] The simulations are initialized using the first-mode analytical solitary wave solution of the stratified Korteweg-de Vries (K-dV) equation in a 900 m deep basin. Such initial field represents a stationary solitary wave in a weakly nonlinear, nonhydrostatic medium, but does not satisfy the system of equations (1) for large amplitude waves. In such a case the nonlinear parameter lies outside the region of applicability of weakly nonlinear models. Once inserted in the numerical scheme, a strong nonlinear wave will evolve in the basin of constant depth. During this evolutional process the initial large amplitude K-dV solitary wave is

modified and a new stationary solitary wave is formed at the front of the wave field. The leading wave, which has a larger phase speed than the wave tail, separates from the tail at a definite stage of its time evolution (corresponding to a travel distance of 20–30 wavelengths from its initial position) and propagates further as an independent internal solitary wave. The model is run until a leading wave separates from the wave tail. This internal solitary wave is then used as initial condition for problem I. This approach was already used in a previous paper [*Vlasenko et al.*, 2000] to study the characteristics of strong ISWs.

[28] Bearing in mind that the wave disturbances in ISW are localized in space, we use "zero" boundary conditions at the lateral "liquid" boundaries, $x = \pm L$, instead of the boundary condition (7). Furthermore, we do not use the equation for the transverse velocity v because we assume that the influence of the rotational effect on the ISWs is negligible.

5.1. Basic Case Simulation

[29] The results of the numerical simulations for the interaction of ISW with the Dreadnought Bank are depicted in Figures 9 and 10. We have assumed in this basic case simulation that the ISW impinging onto the Dreadnought Bank (represented by a triangle) has amplitude of 82 m. The time t is scaled by T, where T is the ratio of the wavelength λ of the ISW to its phase speed c_p. In these simulation runs T has the value 156 s.

[30] The plots depicted in Figure 9 show that the large amplitude ISW interacts strongly with the underwater bank leading to overturning and wave breaking. The rear face of the incoming ISW becomes steeper when it approaches the underwater bank (Figures 9a and 9b). Later, at the rear face of the ISW, the horizontal orbital velocity exceeds the local phase speed and the steep rear wave front outstrips the wave trough (Figure 9c). In this stage, the heavier and denser water penetrates into the relatively light water layers and becomes entrained in the surrounding waters (Figure 9d).

[31] Obviously, zones of internal wave breaking are potential zones of enhanced energy dissipation and intensive diapycnal mixing. Here, the local coefficients of turbulent viscosity and diffusivity increase strongly. In our model these effects are taken into account by the parameterizations (2) and (3). The increase of the local viscosity and diffusion leads to faster attenuation, dissipation and mixing of water layers and to the formation of a local zone with new stable vertical fluid stratification. For more details on internal wave breaking the reader is referred to *Vlasenko and Hutter* [2002a].

[32] Wave breaking generates secondary internal waves (Figure 9e) which propagate in both directions away from the bank (Figure 9f) as transmitted and reflected waves. In Figure 10 the density field anomaly at the time $t = 82T$ is plotted. It clearly shows the strong transmitted internal solitary wave on the left-hand side, and the secondary reflected internal waves on the right-hand side generated during the breaking of the incoming ISW. The leading soliton in the secondary transmitted wave packet has an amplitude of 14 m.

[33] The velocity gradient of the surface current field associated with internal waves is plotted in Figure 11. This gradient determines the modulation depth or the image intensity contrast by which the internal waves become visible on radar images. The image intensity modulation by which internal waves become visible on radar images depends on the velocity gradient of the surface current field associated with internal waves. According to the radar imaging theory of internal waves developed by *Alpers* [1985], the image intensity modulation or modulation depth is, to first order, proportional to the velocity gradient. However, the proportionality factor is highly variable [*Brandt et al.*, 1999]. It depends on radar as well as on several environmental parameters, the most important one being the wind speed and wind direction [*Brandt et al.*, 1999]. The lower the wind speed, the larger is the modulation depth. The gradient of the surface current velocity is plotted in Figure 11. It shows that for the secondary waves it is of the order of 5×10^{-4} s^{-1}, which is well within the range where internal waves become visible on radar images [*Alpers*, 1985; *Brandt et al.*, 1996].

5.2. Sensitivity Runs

[34] The basic case simulation presented in the previous subsection shows how a strong ISW can generate secondary internal waves via wave breaking. However, unanswered questions are: Under what conditions does such a generation take place? How large must the amplitude of the incident ISW be for generating secondary internal waves at the Dreadnought Bank? What parameters control the strong interaction of an ISW with the underwater bank? Some information relevant to these questions can be extracted from *Vlasenko and Hutter* [2002a, 2002b] where the breaking of ISW over a slope shelf topography is investigated, and a criterion for wave breaking is derived. It was found that the depth H_b where the incident ISW with amplitude a_m breaks over a sloping bottom is given by the breaking criterion:

$$H_b = H_m + \frac{a_m}{0.8^\circ/\gamma + 0.4}. \tag{8}$$

Here H_m denotes the depth of maximum wave depression (which is a function of the wave amplitude and water stratification) and γ denotes the inclination angle of the sloping bottom (given in degrees). The position where wave breaking occurs is defined as the position where the horizontal orbital velocity associated with the ISW exceeds its local phase speed.

[35] Criterion (8) was derived for a bottom whose depth decreases linearly with distance. Now we want to apply this criterion to internal wave breaking at the Dreadnought Bank with the aim of determining the minimum ISW amplitude which gives rise to wave breaking. To this end we have carried out several simulations with different ISW amplitudes. The density fields obtained from simulations with amplitudes of 66.3 m, 56.9 m, and 41.7 m are depicted in Figure 12. The plots in the left column refer to the time ($t = 0$) when the ISW breaks just over the top of the bank, and the plots in the right column refer to times when the scattered (and transmitted) internal waves are well developed, which is several tens of wave periods $T = \lambda/c_p$ after wave breaking.

[36] Like in the basic case simulation presented in the last subsection, overturning and wave breaking occurs also

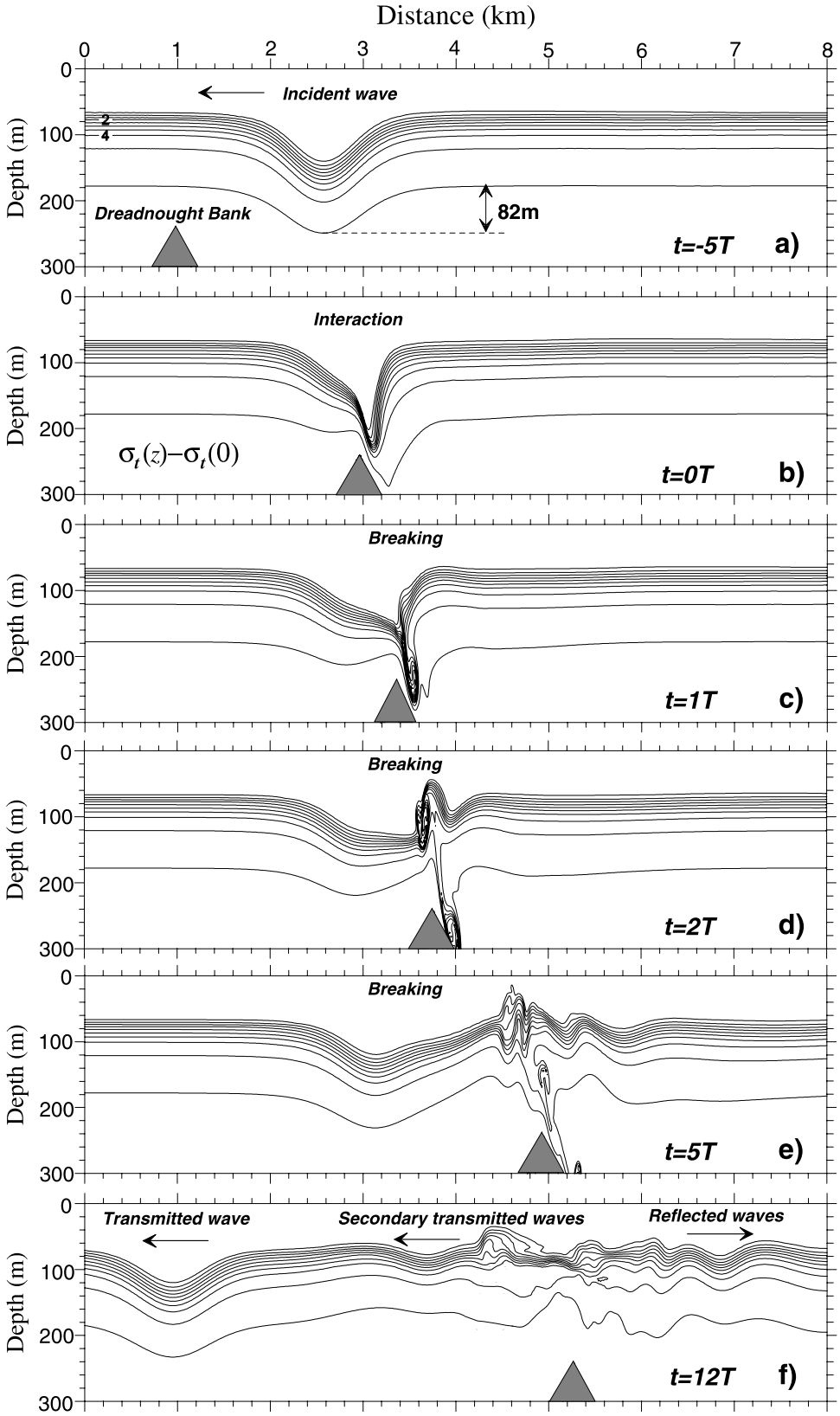

Figure 9. Evolution of the density field during the interaction of an internal solitary wave (ISW) of 82 m amplitude with the Dreadnought Bank (contour interval is 0.5 kg m^{-2}) as calculated from the model. The incoming solitary internal wave and the secondary scattered internal waves (transmitted and reflected) are shown in Figure 9f. The timescale T = 156 s is the ratio of the wavelength of the ISW to its phase speed. The wave field is shown in a moving system of coordinates to illustrate the process of wave breaking in more detail.

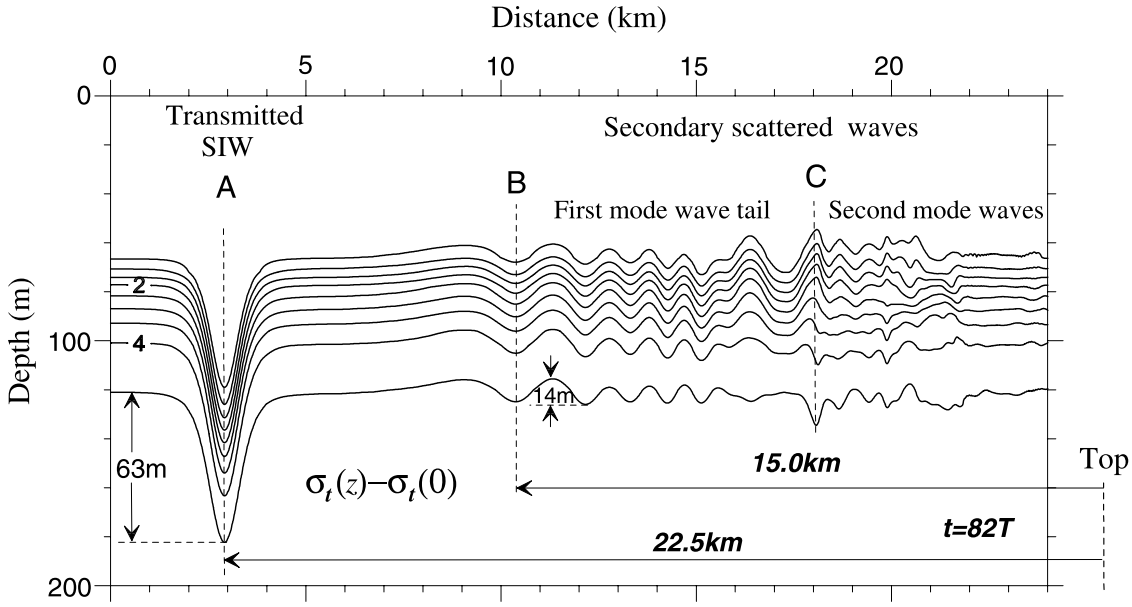

Figure 10. Model result showing the density field anomaly at the time $t = 82T$, which corresponds to the time at which the ERS SAR image depicted in Figure 1 was acquired. The letters A, B, and C denote the positions of the transmitted primary ISW, the leading solitons in the first- and second-mode secondary internal wave packets, respectively. The distances 22.5 km and 15.0 km refer to the distances from the center (top) of the Dreadnought Bank.

when the amplitudes are 66.3 m and 56.9 m, but it does not occur when the amplitude is 41.7 m (Figure 12). Thus the value of minimum amplitude which is sufficient for the generation of secondary internal waves lies in the range between 56.9 m and 41.7 m. This is an unexpected low amplitude, which seems to contradict the breaking criterion (8). If we insert in equation (8) the values H_b = 241 m, $\gamma = 6.84°$ and H_m = 97 m (as used in the basic case simulation), we obtain a_m = 74.4 m. However, there is no contradiction if one remembers that the depth H_m of

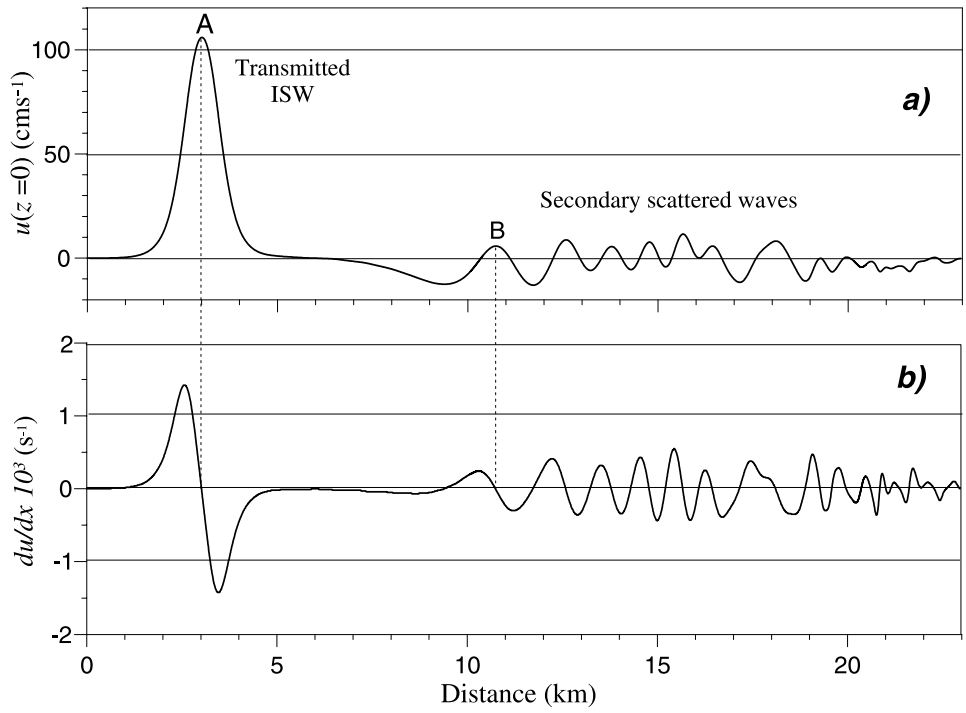

Figure 11. (a) Horizontal component of the surface current velocity induced by the internal solitary waves at the time $t = 82T$. (b) Gradient of this velocity. The positions A and B are the same as in Figure 10.

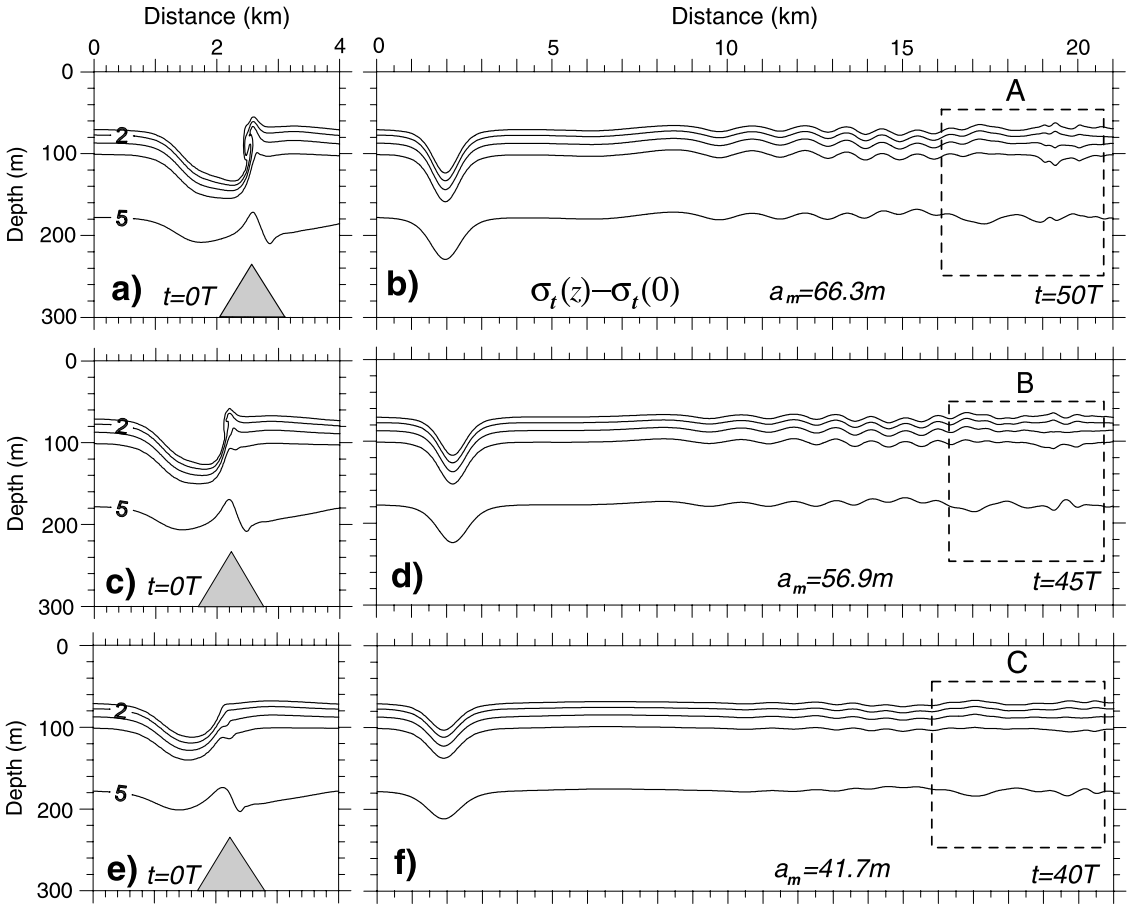

Figure 12. Density fields obtained from simulations with different ISW amplitudes a_m. (top) a_m = 66.3 m. (middle) a_m = 56.9 m. (bottom) a_m = 41.7 m. (left) Refer to the time when the ISW is located over the top of the bank and breaks. (right) Refer to times when the scattered (and transmitted) internal waves are well developed, i.e., at 185 s (Figure 12b), 207 s (Figure 12d), and 255 s (Figure 12f) after wave breaking. The interval between the isolines of density is 1 kg m^{-3}.

the maximum wave depression (which also is a part of equation (8)) also depends on the wave amplitude a_m as shown by *Vlasenko et al.* [2000]. Figure 13 makes this statement more clear. The solid line shows the vertical structure of the first eigenfunction $g(z)$ of the standard boundary value problem

$$g'' + \left(N^2/c_p^2\right)g = 0$$
$$g(0) = g(-H) = 0, \tag{9}$$

which is obtained when the buoyancy frequency profile $N(z)$ given by line 2 in Figure 6 is used. This eigenfunction $g(z)$ is commonly used for the representation of the vertical structure of the Korteveg-de Vries ISW.

[37] As can be seen from Figure 13, the position of the maximum wave depression, H_m, moves closer to the free surface when the wave amplitude a_m increases. In turn, this leads to the widening of the range of the ISW amplitudes which can give rise to wave breaking over the Dreadnought Bank.

[38] The next series of simulations is devoted to the study of the dependence of wave breaking and thus to the generation of secondary internal waves, on bottom inclination and on water stratification, which has an effect on the value of H_m.

[39] According to equation (8) wave breaking occurs at a lower ISW amplitude and at a deeper depth when the bottom slope is steeper. This is confirmed by the simulation results depicted in Figure 14. These simulations were carried with a "shallow" pycnocline as given by the dashed line 1 in Figure 6 and an ISW amplitude a_m of 84 m. For this value of the ISW amplitude the maximum of the pycnocline depression lies at a depth of H_m = 87 m.

[40] Now we want to calculate the minimum inclination angle of the bottom slope at which wave breaking occurs. Substituting into equation (9) the above value for H_m and a_m together with H_b = 241 m, we obtain $\gamma_{\min}$ = 5.5°. The density field obtained for the case $\gamma_{\min}$ = 5.5° is depicted in Figure 14c. We see that weak breaking takes place at the rear face of the ISW. However, as depicted in Figure 14d, it generates a well developed wave tail of secondary scattered waves (of first as well as of second modes). For a steeper slope (γ = 19.1°), wave breaking is much more pronounced (see Figure 14a) and for a gentler slope (γ = 1.6°) wave breaking is absent (see Figure 14e).

[41] The next interesting result of the present study concerns the generation of second-mode internal waves

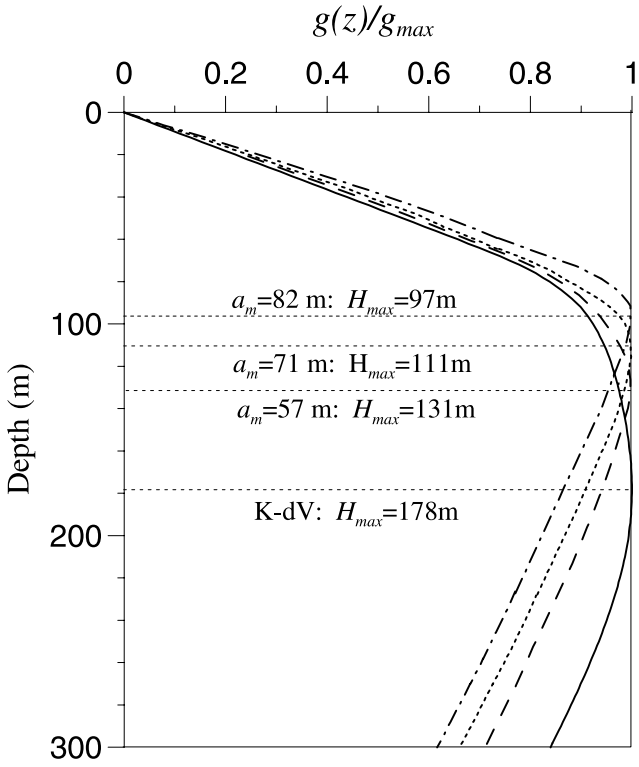

Figure 13. Vertical profiles of the normalized isopycnal displacements calculated at the center of the ISW having amplitudes of 57 m (dashed line), 71 m (dotted line), and 82 m (dash-dotted line). The solid line is the solution of the boundary value problem (9) for the stratification depicted by line 2 in Figure 6.

during the interaction of the ISW of depression with the underwater bank. The counterphase displacement of isopycnals which are characteristic for second-mode internal waves are clearly discernible at the rear side of the scattered wave fields, (see Figure 10, position C, and Figures 12 and 14, dashed rectangles A, B, and C). The generation of second-mode internal waves during the interaction of first-mode internal solitons with a sill was recently observed also in laboratory experiments by *Huettemann and Hutter* [2001] and confirmed in model calculations by *Vlasenko and Hutter* [2001]. Earlier, *Helferich* [1992] already observed in laboratory experiments that multiple turbulent surges, or boluses, generated by breaking of ISW show characteristics of second-mode baroclinic waves.

[42] *Vlasenko and Hutter* [2001] have shown that the basic parameters which control the energy transfer from the first-mode ISW to the high-mode internal waves over the sill is the blocking parameter (in other words: the nondimensional distance from the interface to the top of the sill) and the Froude number (or nondimensional amplitude of the incoming wave). With the increase of these two parameters the efficiency of generation of the second-mode internal waves increases. These results, obtained in laboratory experiments can be transferred to the oceanic scales. As can be seen from comparing the wave fragments A, B and C in Figure 12, the second-mode internal wave has a higher amplitude when wave breaking is stronger.

[43] Another important parameter which influences the structure of the secondary scattered wave train is the bottom inclination. The larger this inclination, the more pronounced are the second-mode internal waves (see Figure 14). The second-mode internal waves are well developed in the case of a steep bottom slope (Figure 14b) and less well in the case of shallow bottom slopes (Figures 14d and 14f).

[44] However, second-mode internal waves can be generated not only by a strong interaction of internal solitary waves with underwater bottom topography involving wave breaking, but also during "laminar" interactions. If the steepness of the bottom topography is large (5°–10° and more) such second-mode waves can also be produced without overturning of the initial ISW.

6. Discussion and Conclusion

[45] It is possible to make quantitative comparisons between distances inferred from the radar image and those obtained from the model calculations. From the ERS SAR image we infer that at the time of the SAR data acquisition the leading soliton of the primary internal solitary wave packet has propagated 22.5 km beyond the center (top) of the Dreadnought Bank. We have used this distance as input for our model calculations with the aim of determining the time it takes for the soliton to travel this distance away from the center of the Dreadnought Bank. Choosing the amplitude of the solitary wave to be 82 m, we obtain for this time $82T = 213$ min. Therefore the phase speed of the transmitted soliton should have been 22.5 km/213 min = 1.76 m s^{-1}, which lies well within the range of measured phase speeds of internal solitons observed in the Andaman Sea. In other parts of the Andaman Sea, *Apel* [1979] measured a phase speed of 2.5 m s^{-1}, *Osborne and Burch* [1980] measured a phase speed of 2.2 m s^{-1}, and *Alpers* [2002] measured a phase speeds between 1.4 and 1.9 m s^{-1}. In Figure 10 the density field is plotted for this time which corresponds to the time of the SAR data acquisition. From this plot the distance between the position of the leading soliton in the secondary internal solitary wave packet and the Dreadnought Bank can be determined. It equals 15 km, which compares well with the measured distance obtained from the SAR image. Depending on direction, this value lies in the range between 15 and 17 km.

[46] Thus the agreement between the model and experimental data strongly supports our hypothesis about the generating mechanism of secondary internal waves observed in the area of the Dreadnought Bank: a secondary internal wave packet was generated by scattering of a large-amplitude internal solitary wave interacting with the underwater bank.

[47] We have assumed in our model calculations that only the leading soliton of the incident wave packet generates the secondary wave packet. A justification of this assumption is that the subsequent solitons in a wave packet have usually much smaller amplitudes which do not lead to wave breaking and thus do not generate secondary internal waves (see discussion in section 5.2).

[48] Since our model is a 2-D model, three-dimensional effects, like radial spreading of the secondary wave field, are not described. However, it is evident that radial spreading causes additional attenuation; the wave amplitude decreases

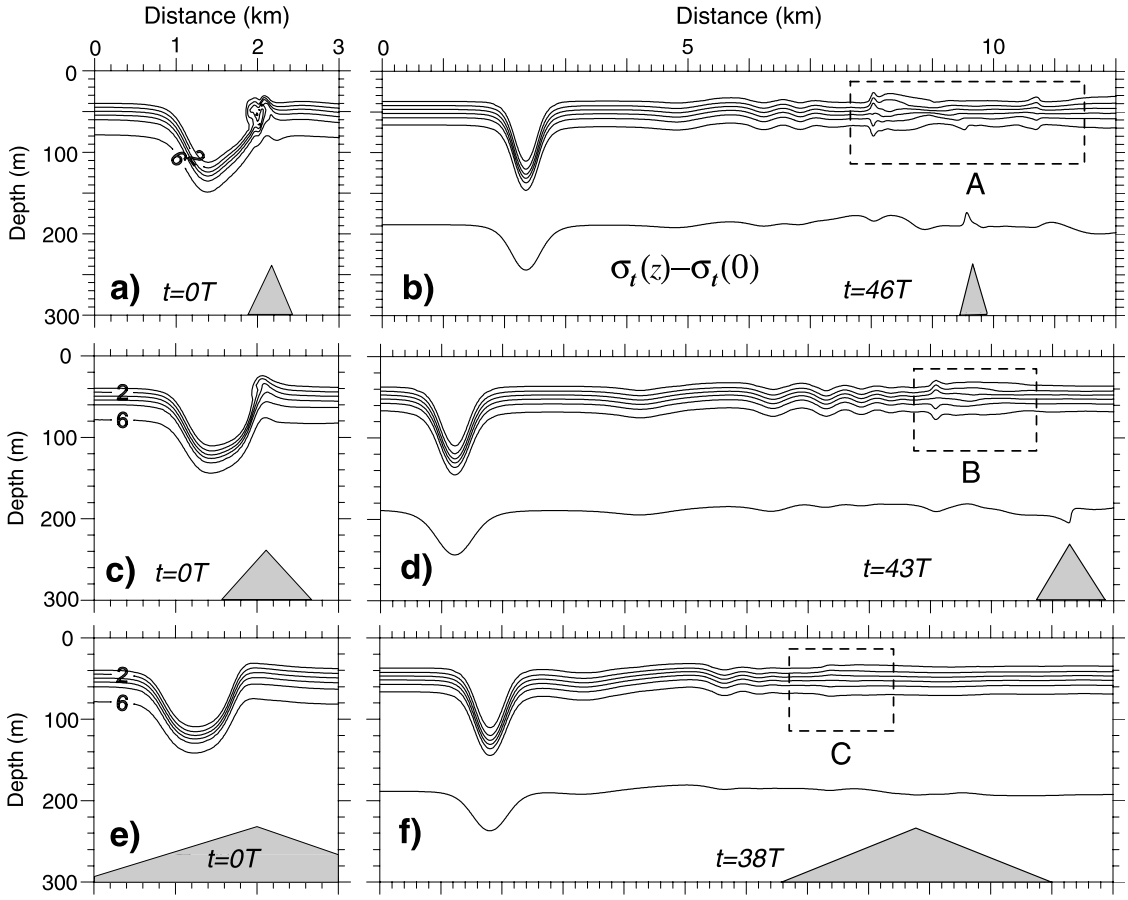

Figure 14. Same as Figure 12, but with different bottom inclinations γ: (top) γ = 19.1°; (middle) γ = 6.8°; and (bottom) γ = 1.6°. The density fields were calculated for the fluid stratification given by line 1 in Figure 6, and the ISW amplitude was the held constant at a_m = 84 m. The timescale is T = 75 s.

with distance according to spreading law $A(r) = A_0(r/r_0)^{-1/2}$ [*Maxworthy*, 1980; *Ramirez et al.*, 2002]. Thus the wave amplitudes of the secondary waves must be smaller than the one calculated from our 2-D model.

[49] Unfortunately, only one ERS SAR image could be presented in this paper. This shows sea surface manifestations of secondary internal waves suggesting generation by the interaction of a large-amplitude internal solitary wave with the Dreadnought Bank. In the archive of the Centre for Remote Imaging, Sensing and Processing (CRISP) at the National University of Singapore (see http://crisp.nus.edu.sg/crisp_cat.html) we have found only 9 sets of ERS-1 and ERS-2 SAR images acquired over this sea area (frames 3465 and 3483). They were acquired in the period between 1 April 1996 and 5 January 2002. Only the one acquired on 11 February 1985 (Figures 1 and 2) shows these features. However, this is not surprising, since we expect that secondary internal waves are generated only when large-amplitude ISWs impinge on the Dreadnought Bank, which should be the case only during spring tides. Furthermore, the SAR data acquisition must take place 2–4 hours after the ISWs have hit the bank, otherwise the amplitudes of the secondary waves have attenuated so much that the sea surface manifestations are too weak to be detectable on the SAR images. Thus the chances are very low to acquire spaceborne SAR images over this site at these very specific times. (Note that the ERS satellites pass over the same area only every 35 days and that not always the SAR is switched on over this site.)

[50] We have searched in the archives of the ERS receiving stations at Singapore and at Chungli, Taiwan (see http://www.csrsr.ncu.edu.tw/english.ver/query.htm) for others examples of secondary internal waves generated by the interaction of an ISW with an underwater obstacle. So far we have found sea surface manifestations of circular internal wave patterns adjacent to sea surface manifestations of large-amplitude ISWs only in the Sulu Sea around the Bancoran Island, which lies on the top of a coral reef at 70°58′N, 180°40′E. One example of such an ERS SAR image can be found at University of Hamburg homepage (see http://www.ifm.uni-hamburg.de/ers-sar/Sdata/oceanic/intwaves/sulusea/247263411-3429-3447-3465ERS1.html). In the archive of the receiving station in Singapore one can find three more examples of sets of ERS SAR images showing such features in this sea area (acquired on 13 April 1998, 24 November 1997, and 22 July 1996; frames 3447, 3465).

[51] When comparing the sea surface manifestations of the secondary internal waves visible on the ERS-2 SAR image of 11 February 1997 (Figures 1 and 2) with our model calculations, an unanswered question remains: Why has the quasicircular wave pattern an asymmetric shape

(more waves propagate eastward than westward)? This observation can very likely be explained by one or a combination of the following effects: (1) the Dreadnought bank has an asymmetric shape which potentially leads to refraction and asymmetric wave pattern (see discussion in section 4.2); (2) an along-slope Lagrangian current generated by an incident ISW propagating on a sloping bottom can give rise to an asymmetric wave pattern by wave reflection [*Thorpe*, 1997] or wave breaking [*Thorpe*, 1999]; and (3) the initial horizontal momentum of the incident ISW very likely has an effect on the directional distribution of the radiated wave field. As shown by *Vlasenko and Hutter* [2002a], wave breaking over a bank leads to horizontal intrusion of water, which propagates upstream. This could be an explanation why the radiated energy is concentrated in a narrow segment in the wave propagation direction of the incident ISW and why it does not attenuate rapidly as radial spreading would suggest.

Appendix A: Two-Layer Model of Internal Waves Generation and Propagation Over the Dreadnought Bank

[52] The linear system of equations describing two-dimensional internal waves (x, y plane) in a two-layer fluid has the form

$$\begin{gathered} U_{1t} - fV_1 = -\rho_1^{-1}P_{1x}, \\ V_{1t} + fU_1 = -\rho_1^{-1}P_{1y}, \\ (\xi_1 - \xi_2)_t + H_1(U_{1x} + V_{1y}) = 0, \\ P_1 = g\rho_1(\xi_1 - z), \\ U_{2t} - fV_2 = -\rho_2^{-1}P_{2x}, \\ V_{2t} + fU_2 = -\rho_2^{-1}P_{2y}, \\ \xi_{2t} + H_2(U_{2x} + V_{2y}) + U_2H_{2x} + V_2H_{2y} = 0, \\ P_2 = g\rho_1(\xi_1 - \xi_2 + H_1) + g\rho_2(\xi_2 - z - H_1). \end{gathered} \tag{A1}$$

Here z is the vertical coordinate; U_i,V_i, are the horizontal velocity components, P_i is the hydrostatic pressure; ρ_i is the density; H_i is the water depth; $i = 1, 2$ is the layer number; f is the Coriolis parameter; ξ_1 and ξ_2 are the deviations of the free surface and the interface from their equilibrium values, respectively. Taking into account the tidal periodicity of the wave motions,

$$\{\xi_i, U_i, V_i\} = \{\zeta_i, u_i, v_i\}\exp(-i\sigma t)$$

(σ is the tidal frequency), and introducing new variables as follows $\eta_1 = \zeta_1$, $\eta_2 = \varepsilon\zeta_2 + \gamma\eta_1$, where $\gamma = \rho_1/\rho_2$, $\epsilon = 1 - \gamma$, the system of equations (A1) can be reduced to the following form:

$$\begin{gathered} H_1\left(\eta_{1xx} + \eta_{1yy}\right) + \left(\sigma^2 - f^2\right)(\eta_1 - \eta_2)/g\varepsilon = 0 \\ H_2\left(\eta_{2xx} + \eta_{2yy}\right) + if\left(H_{2x}\eta_{2y} - H_{2y}\eta_{2x}\right)/\sigma \\ + H_{2x}\eta_{2x} + H_{2y}\eta_{2y} + \left(\sigma^2 - f^2\right)(\eta_2 - \gamma\eta_1)/g\varepsilon = 0. \end{gathered} \tag{A2}$$

This system of equations describes free propagating surface and interfacial waves in a two-layer fluid. External forcing is introduced in the system of equations (A2) by a barotropic or baroclinic tidal wave interacting with a varying bottom topography. In this case the solution of system (A2) can be represented as the superposition of an incident wave propagating at angle θ relative to the x axis and a scattered surface wave χ_1 or a scattered interfacial wave χ_2 as follows:

$$\begin{aligned} \eta_1 &= \chi_1 + A_0\exp[ik(x\cos\theta + y\sin\theta)] \\ \eta_2 &= \chi_2 + A_0\left[1 - k^2gH_1\left(\sigma^2 - f^2\right)^{-1}\varepsilon\right] \\ &\quad \times \exp[ik(x\cos\theta + y\sin\theta)]. \end{aligned} \tag{A3}$$

Here A_0 and A_0 $[1 - k^2gH_1(\sigma^2 - f^2)^{-1}\varepsilon]$ denote the amplitudes of the incident wave at the free surface and at the interface, respectively, and k denotes the wave number:

$$k = \frac{H_1 + H_2 \pm \sqrt{(H_1 + H_2)^2 - 4H_1H_2\gamma}}{2gH_1H_2\gamma}\left(\sigma^2 - f^2\right).$$

The "+" sign in the last equation applies to the internal wave, and the "−" sign to the barotropic wave. After substitution of (A3) into (A2), we obtain two inhomogeneous elliptic equations for the wave disturbances χ_1 and χ_2, which can be solved numerically (e.g., by the Gauss-Zeidels iteration procedure). A square computational area (150 km × 150 km) with a rectangular grid and a spatial step of 1 km is used. Owing to the fact that the wave amplitude decrease with distance from its source because of radial divergence, we can set $\chi_1 = 0$ and $\chi_2 = 0$ at the lateral fluid boundaries.

[53] **Acknowledgments.** The authors wish to thank Nataliya Stashchuk and Len Wood for their helpful remarks. The comments of two anonymous reviewers and an Associate Editor greatly improved the manuscript.

References

Alpers, W. (1985), Theory of radar imaging of internal waves, *Nature*, *314*, 245–247.

Alpers, W. (2002), Shoaling of internal solitary waves in the Andaman Sea studied by space-borne SAR imagery and in-situ measurements, report, Inst. of Oceanogr. Univ. of Hamburg, Germany.

Apel, J. R. (1979), Observations of internal wave surface signatures in ASTP photographs, *NASA Spec. Publ.*, *SP-412*, 505–509.

Apel, J. R., J. R. Holbrock, A. K. Liu, and J. J. Tsai (1985), The Sulu Sea internal soliton experiment, *J. Phys. Oceanogr.*, *15*, 1625–1651.

Brandt, P., W. Alpers, and J. O. Backhaus (1996), Study of the generation and propagation of internal waves in the Strait of Gibraltar using a numerical model and synthetic aperture radar images of the European ERS-1 satellite, *J. Geophys. Res.*, *101*, 14,237–14,252.

Brandt, P., A. Rubino, W. Alpers, and J. O. Backhaus (1997), Internal waves in the Strait of Messina studied by a numerical model and synthetic aperture radar images from the ERS-1/2 satellites, *J. Phys. Oceanogr.*, *27*, 648–663.

Brandt, P., R. Romeiser, and A. Rubino (1999), On the determination of characteristics of the interior ocean dynamics from radar signatures of internal solitary waves, *J. Geophys. Res.*, *104*, 30,039–30,047.

Casulli, V., and G. S. Stelling (1998), Numerical simulations of 3-D quasi-hydrostatic, free-surface flow, *J. Hydraul. Eng.*, *124*, 678–686.

Cummins, P. F., J. Y. Cherniawsky, and M. G. G. Foreman (2001), North Pacific internal tide from the Aleutian Ridge: Altimeter observations and modeling, *J. Mar. Res.*, *59*, 167–191.

Diebels, S., B. Schuster, and K. Hutter (1994), Nonlinear internal waves over variable topography, *Geophys. Astrophys. Fluid Dyn.*, *76*, 165–192.

Gerkema, T., and J. T. F. Zimmermann (1995), Generation of nonlinear internal tides and solitary waves, *J. Phys. Oceanogr.*, *25*, 1081–1094.

Helferich, K. R. (1992), Internal solitary wave breaking and run-up on a uniform slope, *J. Fluid Mech.*, *243*, 133–154.

Holloway, P. E., and M. A. Merrifield (1999), Internal tide generation by seamounts, ridges, and islands, *J. Geophys. Res.*, *104*, 25,937–25,951.

Huettemann, H., and K. Hutter (2001), Baroclinic solitary water waves in a two-layer system with diffusive interface, *Exper. Fluid*, *30*, 317–326.

Kao, T. W., F.-S. Pan, and D. Renouard (1985), Internal solitons on the pycnocline: Generation, propagation, and shoaling and breaking over a slope, *J. Fluid Mech.*, *159*, 19–53.

Lamb, K. G. (1994), Numerical experiments of internal wave generation by strong tidal flow across a finite amplitude bank edge, *J. Geophys. Res.*, *99*, 843–864.

Levitus, S., and T. P. Boyer (1994), *World Ocean Atlas 1994*, vol. 4, *Temperature*, *NOAA Atlas NESDIS 4*, 129 pp., Natl. Oceanic and Atmos. Admin., Silver Spring, Md.

Levitus, S., R. Burgett, and T. P. Boyer (1994), *World Ocean Atlas 1994*, vol. 3, *Salinity*, *NOAA Atlas NESDIS 3*, 111 pp., Natl. Oceanic and Atmos. Admin., Silver Spring, Md.

Liu, A. K., Y. S. Chang, M.-K. Hsu, and N. K. Lang (1998), Evolution of nonlinear internal waves in the East and South China Seas, *J. Geophys. Res.*, *103*, 7995–8008.

Mahadevan, A., J. Oliger, and R. Street (1996), A non-hydrostatic mesoscale ocean model. part 2: Numerical implementation, *J. Phys. Oceanogr.*, *26*, 1881–1900.

Marshall, J., A. Adcroft, C. Hill, L. Perelman, and C. Heisey (1997), A finite-volume, incompressible Navier Stokes model for studies of the ocean on parallel computers, *J. Geophys. Res.*, *102*, 5753–5766.

Maxworthy, T. (1979), A note on the internal solitary waves produced by tidal flow over a three-dimensional ridge, *J. Geophys. Res.*, *84*, 338–346.

Maxworthy, T. (1980), On the formation of nonlinear internal waves from the gravitational collapse of mixed regions in two and three dimensions, *J. Fluid Mech.*, *96*, 47–64.

Niwa, Y., and T. Hibiya (2001), Numerical study of the spatial distribution of the M_2 internal tide in the Pacific Ocean, *J. Geophys. Res.*, *106*, 22,441–22,449.

Osborne, A. R., and T. L. Burch (1980), Internal solitons in the Andaman sea, *Science*, *208*, 451–460.

Osborne, A. R., T. L. Burch, and R. I. Scarlet (1978), The influence of internal waves on deep-water drilling, *J. Pet. Tech.*, *30*, 1497–1504.

Pakanowski, R. C., and S. G. H. Philander (1981), Parameterisation of vertical mixing in numerical models of tropical oceans, *J. Phys. Oceanogr.*, *11*, 1443–1451.

Perry, R. B., and G. R. Shimke (1965), Large amplitude internal waves observed off the northwest coast of Sumatra, *J. Geophys. Res.*, *70*, 2319–2324.

Ramirez, C., D. Renouard, and Y. A. Stepanyants (2002), Propagation of cylindrical waves in a rotating fluid, *Fluid Dyn. Res.*, *30*, 169–196.

Sandstrom, H., and N. S. Oakey (1995), Dissipation in internal tides and solitary waves, *J. Phys. Oceanogr.*, *25*, 604–614.

Stacey, M. W., and L. Zedel (1986), The time-dependent hydraulic flow and dissipation over the sill of Observatory Inlet, *J. Phys. Oceanogr.*, *16*, 1062–1076.

Thorpe, S. A. (1997), On the interaction of internal waves reflecting from slopes, *J. Phys. Oceanogr.*, *27*, 2072–2078.

Thorpe, S. A. (1999), The generation of alongslope currents by breaking internal waves, *J. Phys. Oceanogr.*, *29*, 29–38.

Vlasenko, V., and K. Hutter (2001), Generation of second mode solitary waves by the interaction of first mode soliton with a sill, *Nonlinear Processes Geophys.*, *8*, 223–239.

Vlasenko, V., and K. Hutter (2002a), Numerical experiments on the breaking of solitary internal waves over a slope-shelf topography, *J. Phys. Oceanogr.*, *32*, 1779–1793.

Vlasenko, V., and K. Hutter (2002b), Transformation and disintegration of strongly nonlinear internal waves by topography in stratified lakes, *Ann. Geophys.*, *20*, 2087–2103.

Vlasenko, V., P. Brandt, and A. Rubino (2000), On the structure of large amplitude internal solitary waves, *J. Phys. Oceanogr.*, *30*, 2172–2185.

Vlasenko, V., N. Stashchuk, and K. Hutter (2002), Water exchange in fjords induced by tidally generated internal lee waves, *Dyn. Atmos. Oceans*, *35*, 63–89.

Wallace, B. C., and D. L. Wilkinson (1988), Run-up of internal waves on a topographic sill in a two-layered system, *J. Fluid Mech.*, *191*, 419–442.

Wessels, F., and K. Hutter (1996), Interaction of internal waves with a topographic sill in a two-layered fluid, *J. Phys. Oceanogr.*, *26*, 5–20.

W. Alpers, Zentrum für Meeres- und Klimaforschung, Institut für Meereskunde, Universität Hamburg, Bundesstrasse 53, D-20146 Hamburg, Germany. (alpers@ifm.uni-hamburg.de)

V. Vlasenko, School of Earth, Ocean and Environmental Sciences, University of Plymouth, Drake Circus, PSQ A504, Plymouth PL4 8AA, UK. (vvlasenko@plymouth.ac.uk)